Changes in Groundwater Level Possibly Encourage Shallow Earthquakes in Central Australia: The 2016 Petermann Ranges Earthquake

Shuai Wang[1,2] (iD), Wenbin Xu[1] (iD), Caijun Xu[2] (iD), Zhi Yin[3] (iD), Roland Bürgmann[4] (iD), Lin Liu[5] (iD), and Guoyan Jiang[5] (iD)

[1]Department of Land Surveying and Geo-informatics, The Hong Kong Polytechnic University, Hong Kong, China, [2]School of Geodesy and Geomatics, Wuhan University, Wuhan, China, [3]Institute of Geodesy, University of Stuttgart, Stuttgart, Germany, [4]Berkeley Seismological Laboratory and Department of Earth and Planetary Science, University of California, Berkeley, California, USA, [5]Earth System Science Program, Faculty of Science, The Chinese University of Hong Kong, Hong Kong, China

Abstract The mechanisms of unusual shallow intraplate earthquakes that occasionally occur in stable cratons remain poorly understood. Here we analyze coseismic and postseismic displacement fields associated with the 2016 Petermann Ranges earthquake in central Australia using interferometric synthetic aperture radar data. The earthquake ruptured a previously unmapped fault and was dominated by thrust slip motion of up to 95 cm within the top 3 km of the crust. Postseismic deformation analysis suggests that a combination of poroelastic rebound and afterslip are responsible for the observed signals. The inferred afterslip overlapping spatially with the coseismic rupture highlights that the postseismic slip is coupled with the pore fluid flow around the fault zones. Analysis of historic groundwater-level changes suggests that shallow seismicity around the Petermann Ranges may have been triggered by environmental stress perturbations due to the fluctuations of groundwater level; however, it is not easy to document statistical significance of this correlation.

Plain Language Summary Shallow surface-rupturing earthquakes have been observed globally. However, how these events are triggered and why they sometimes occur within stable continents is largely unknown. We carefully study the coseismic and postseismic deformation of a 2016 M_w 6 earthquake in central Australia to determine the source parameters and slip distributions. We find the coseismic slip and early afterslip are concentrated at depths shallower than 3 km, and poroelastic rebound substantially contributes to the early period of postseismic deformation. We further investigate potential mechanisms to explain rock failure at such shallow depth and find a possible relationship between the fluctuations of groundwater level and the occurrence of shallow seismicity in the region. The results of this study help shed light on the processes and causes of shallow earthquakes.

1. Introduction

Earthquakes are a manifestation of lithospheric deformation and usually occur in tectonically active zones, such as the major tectonic boundaries and more distributed deformation zones (Gordon, 1998). Thanks to rapidly advancing seismic and geodetic observation techniques, such as interferometric synthetic aperture radar (InSAR) and the Global Navigation Satellite System (GNSS), scientists find increasing evidence of moderate to large shallow earthquakes in stable continental interiors (Dawson et al., 2008). Different from the tectonically active zones, the stable continents hosting these events (e.g., the Australian continent and central Africa) are located far from the plate boundaries and often show negligible geodetic strain accumulation rates (Calais et al., 2016). However, the occurrence of earthquakes in these low strain rate regions indicates that stress levels in these areas are near critical (Calais et al., 2016). This combination of extremely low background stress accumulation rates and near-critical stress levels suggests that such intraplate earthquakes in the stable interiors are often triggered by transient local stress perturbations or fault strength variations due to a variety of possible external environmental changes (Calais et al., 2016).

Located far from active plate boundaries, the low-relief Australian continent (Pain et al., 2012) is generally deemed of relatively low seismic hazard compared to other parts of the Earth. However, a number of $2 \leq M \leq 6$ earthquakes still occur in the Australian continent (Leonard et al., 2014). A majority of these
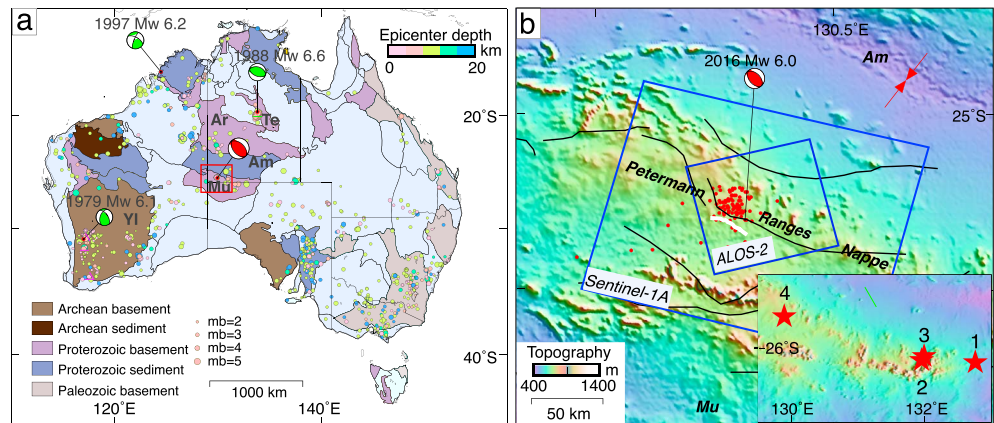
Figure 1. Tectonic settings. (a) Red beach ball is the GCMT solution of the 2016 Petermann Ranges earthquake; green ones represent three historical $M_w > 6$ earthquakes. Small circles represent $M \geq 2$ earthquakes since 1910 (https://earthquake.usgs.gov/) and color-coded by their focal depths. Ar, Arunta Block; Am, Amadeus Basin; Mu, Musgrave Block; Te, Tennant Creek Inlier; YI, Yilgarn Block. Red rectangular box outlines the study area shown in (b). (b) Fault map surrounding the 2016 event. Blue boxes outline the spatial coverage of the SAR data. Black lines delineate regional major faults. Thick white line represents the 2016 fault rupture identified from InSAR data. Red circles represent aftershocks from the ISC within 30 days after the main shock. Red arrows indicate the regional maximum horizontal stress orientation (Rajabi et al., 2017). Red stars in the inset map represent the historical surface faulting earthquakes recorded in Petermann Ranges (Table S1; Clark & McPherson, 2013; Clark et al., 2014).

intraplate events are distributed in the southwest and southeast of Australia, areas that are characterized by Archean and Paleozoic basements, respectively (Figure 1a). Meanwhile, some events occurred in central Australia which is characterized by early Paleozoic tectonic features in Proterozoic basements. In central Australia, the Petermann Ranges contain a Cambrian-age imbricate thrust system that forms the boundary between the Amadeus basin and Musgrave block (Davidson, 1973). Analysis of gravity and magnetic data indicates uplift of the crust–mantle boundary beneath the Petermann Ranges, which suggests a thinner and stronger crust compared to the surrounding lithosphere (e.g., Aitken et al., 2009). However, the Petermann Ranges have experienced four moderate ($M_w > 5$) earthquakes in the past 35 years (Figure 1b), indicating that faults here are critically stressed.

On 20 May 2016 (UTC 18:14:04), a M_w 6.0 earthquake struck a sparsely inhabited region within the Petermann Ranges (Figure 1b). This earthquake is the largest event ever instrumentally recorded in the region, with the hypocenter determined at a very shallow depth (approaches to 0 km) by Geoscience Australia. Field investigations found that this earthquake generated clear surface breaks and fault scarps (Gold et al., 2017; King et al., 2018). A coseismic slip model was proposed by Polcari et al. (2018), but their strike-fixed fault model is too simple to explain the complex near-fault observations. The postseismic deformation and its underlying mechanisms have not been reported yet. More importantly, the occurrence of unusual shallow intraplate earthquakes in stable Australia remain poorly understood in terms of why and how these events are caused. Therefore, we undertake this investigation to improve our understanding of the potential mechanism responsible for the shallow seismicity in stable Australia.

Here we use InSAR data to generate coseismic displacement maps and invert for a detailed coseismic distributed slip model (e.g., Massonnet et al., 1993; Xu, 2017; Xu et al., 2018). We calculate the postseismic transient displacement signals to study the mechanisms of postseismic deformation. Finally, we estimate temporal changes of groundwater level from both Gravity Recovery and Climate Experiment (GRACE; Wahr et al., 1998) and well data to assess whether recent environmental changes could be responsible for the shallow seismicity in Australia.

2. Data and Inversion Method

2.1. Data

The coseismic displacements of the Petermann earthquake were captured by the L-band Advanced Land Observing Satellite 2 (ALOS-2) from an ascending orbit and C-band Sentinel-1 descending-track

acquisitions (Table S2). These observations provide us a unique opportunity to shed light on the mechanism of the earthquake, given the limited ground-based geodetic measurements and sparsely distributed seismic network near the epicenter. To examine the temporal evolution of the postseismic displacement signals, 21 Sentinel-1 SAR images spanning from 1 June 2016 to 14 June 2017 were also analyzed (Table S3). In addition, we processed a pair of ascending ALOS-2 data acquired between 14 June 2016 and 28 November 2017 to obtain cumulative postseismic displacements from a second viewing geometry (Table S4). Detailed InSAR data processing steps are described in the supporting information (Text S1; see also Berardino et al., 2002; Jónsson et al., 2002; Schmidt & Bürgmann, 2003; Wang et al., 2017).

2.2. Inversion Method

To better understand the fault geometry and slip distribution of the 2016 Petermann earthquake, we used a triangular dislocation model (Meade, 2007) to model the coseismic interferograms, which allows us to describe a complex realistic fault surface without any dislocation gaps and overlaps (e.g., Huang et al., 2017; Yin et al., 2016). Based on the identified fault surface trace from the ALOS-2 interferogram (Figure 2), we built a strike-variable fault model by using the method proposed by Yin et al. (2016). To account for the rupture complexities in the near-field, the size of the fault patches was set to be small (~200 m) near the surface and the fault model consists of 1,032 discrete triangular patches in total (Figure 2g). We searched for the optimal uniform dip angle for which the root-mean-square (RMS) error reaches a minimum (Figure S5b) (e.g., Wang et al., 2017). A nonnegative least squares inversion method and a scale-dependent umbrella Laplacian smoothing constraint were applied in the inversion (Maerten et al., 2005).

Aseismic afterslip, poroelastic rebound, and viscoelastic relaxation are three fundamental mechanisms responsible for postseismic deformation (e.g., Zhao et al., 2017). Considering that postseismic deformation is strongly localized with high gradients near fault bends, as well as the low magnitude, shallow depth, and cratonic setting of the 2016 event, we considered afterslip and poroelastic rebound to be the only relevant mechanisms that contribute to the postseismic deformation. We assumed that postseismic afterslip and poroelastic rebound were effectively completed by the end of the Sentinel-1 observation period (390 days after the earthquake; Figure S4) and jointly considered both ALOS-2 and Sentinel-1 data sets as representing total postseismic deformation since 12 and 25 days after the main shock, respectively.

In the postseismic slip modeling, the same fault model and inversion strategies were followed as in the coseismic slip modeling. The poroelastic rebound induced surface deformation was calculated by differencing the coseismic displacements modeled under fully drained and undrained conditions, respectively (Jónsson et al., 2003). Considering the lack of accurate information about the actual hydrological parameters in the study area, we fixed the Poisson's ratio to be 0.25 for the drained condition and performed several calculations in which the value of Poisson's ratio for undrained condition is varied (Figures S8 and S9). The difference in Poisson's ratios for the drained and undrained conditions is optimally determined when the observed cumulative displacement is best fit. The detailed coseismic and postseismic slip inversion steps are described in the supporting information (Text S2; see also Jónsson et al., 2003; Maerten et al., 2005; Parsons et al., 2006; Xu, 2017).

3. Results

3.1. Coseismic Deformation Maps and Slip Model

The coseismic deformation pattern as revealed by the ALOS-2 interferogram differs significantly on either side of the fault. The hanging wall is dominated by motion toward the satellite in the radar line-of-sight (LOS) direction close to the fault (Figure 2), while little deformation is seen on the footwall. This suggests that it was a shallow thrusting event (e.g., Dawson et al., 2008), with the causative fault dipping to the northeast. A clear 24-km-long arcuate surface rupture is identified from the phase discontinuity of the ALOS-2 interferogram (Figures 2a and S1). The maximum LOS displacement is ~80 cm for the ALOS-2 data but is only ~20 cm for the Sentinel-1 data due to decorrelation in the near-field signal (Figure 2d). In addition, the 2016 event appears to have triggered slip of several secondary surface faults in the hanging wall, resulting in clear phase discontinuities (Figure S2).
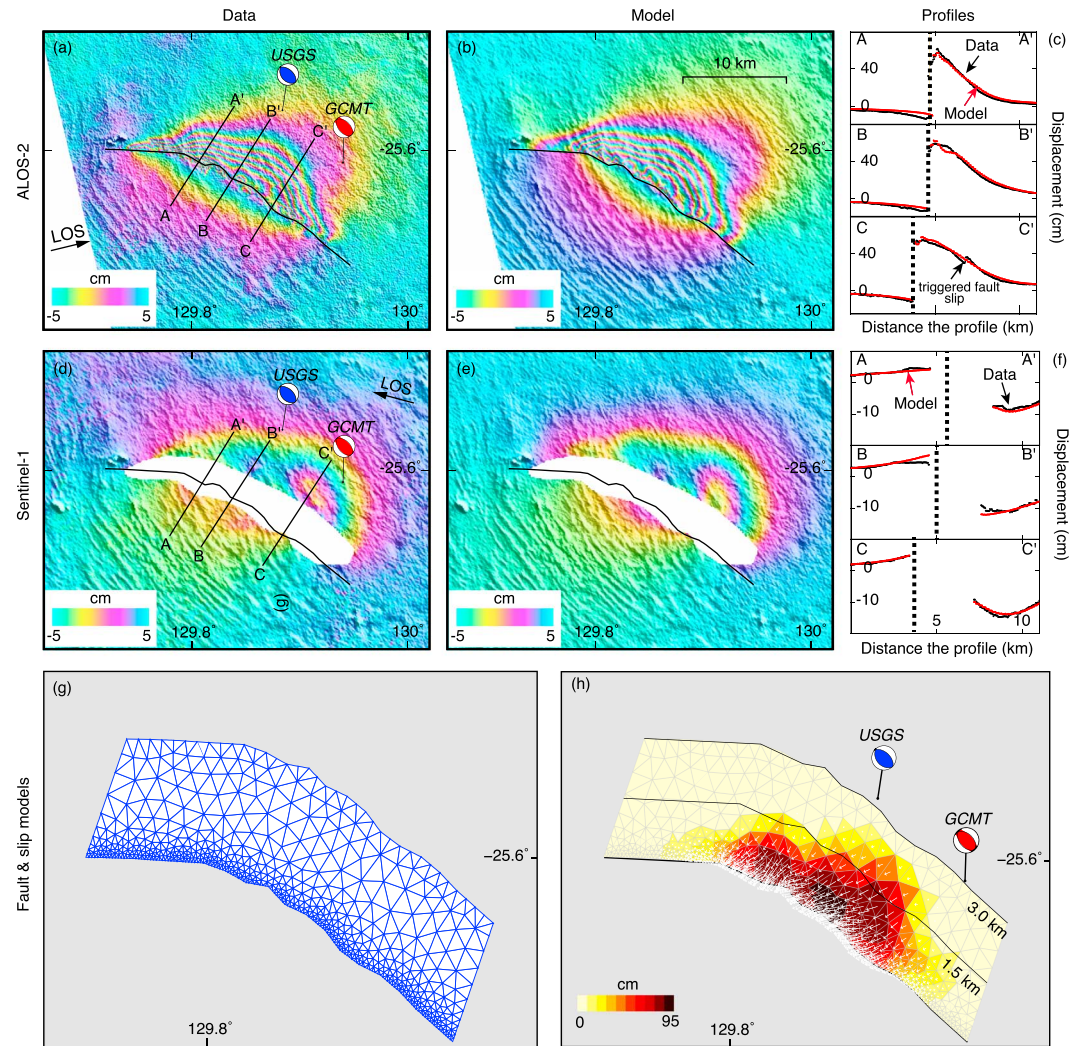
Figure 2. Observed and modeled coseismic displacements due to the 2016 Petermann Ranges earthquake. (a) Observed LOS displacement from the ALOS-2 ascending track 124. The unwrapped phase is rewrapped with a fringe interval of −5 to 5 cm. Black curved line represents the identified surface trace from the ALOS-2 coseismic deformation map. (b) Corresponding model prediction. (c) Observed (black) and modeled (red) displacements along the three profiles shown in (a). Black dashed line represents the fault location. (d–f) Same as (a) and (b) but from the Sentinel-1 descending track 75. The near-field is masked out due to the loss of coherence caused by the high LOS gradients. (g) The fault geometry model with surface meshed by triangle elements. (h) The optimal coseismic slip model. White arrows show the slip direction of the hanging wall. The colors represent the slip amplitude.

The optimal coseismic slip model shows that the causative fault dips gently (22°) to the northeast and is dominated by thrust motion with a minor sinistral shearing component (Figure 2h), which is consistent with the regional maximum horizontal stress orientation (Figure 1b). The earthquake is characterized by one asperity with a maximum slip of 95 cm concentrated at shallow depths between 0 and 3 km. This shallow distributed coseismic slip is a robust feature as documented in Figure S7, which shows that the coseismic slip distribution does not change significantly when a larger depth extent (5 km) fault model is used. Our optimal slip model (Figure 2h) yields a geodetic moment of 1.50×10^{18} N m and explains the prominent ground deformation better than that inverted using a simple strike-fixed fault model (Polcari et al., 2018). Without considering the fault bends, Polcari et al.'s model shows a poor fit to the near-field observations, especially those at the western end of the fault. Localized residuals are seen close to small-scale fault bends within an ~1-km-wide zone due to heterogeneous shallow slip and possible inelastic off-fault ground deformation (Figure S2).
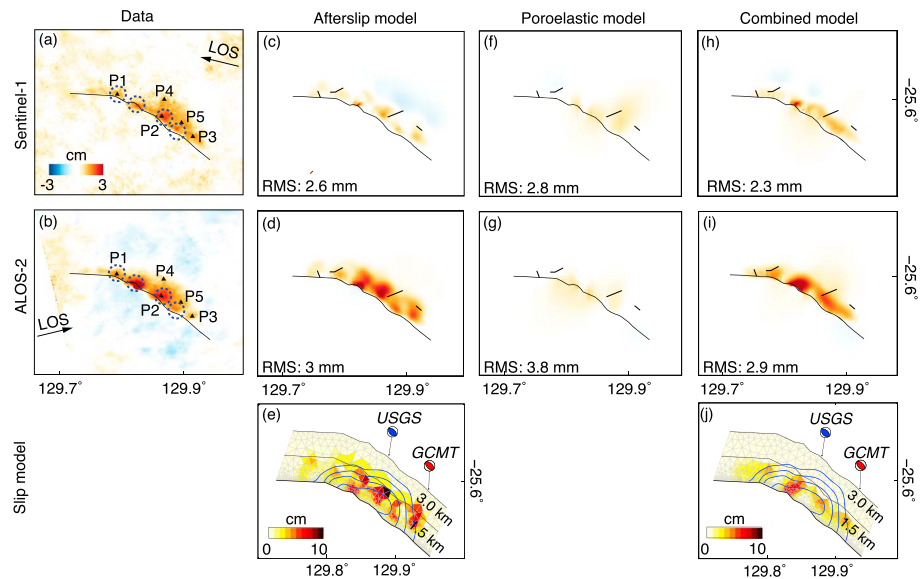
Figure 3. Cumulative postseismic displacements from (a) descending Sentinel-1 (12–390 days) and (b) ascending ALOS-2 data (25–557 days). Solid triangles denote the selected near-field pixels (P1–P5). Dashed circles outline the localized deformation regions near fault bends that could be related to poroelastic rebound. Afterslip model prediction in (c) descending and (d) ascending orbits, respectively. Black short lines in (c and d) represent the identified secondary coseismic fault offsets. (e) Afterslip distribution model. Thin blue contours represent the coseismic slip with an interval of 20 cm. (f and g) poroelastic model predictions. (h–j) Same as in (c–e) but for the combined model.

3.2. Postseismic Deformation and Model Results

3.2.1. Postseismic Deformation

Figures 3a and 3b show the cumulative postseismic LOS displacements observed from the descending Sentinel-1 and ascending ALOS-2 data, respectively. The deformation pattern is similar to that of the coseismic rupture with dominant hanging wall uplift and is characterized by high gradients close to the fault bends. Figure S4c shows the LOS displacement time series at selected pixels. The time decaying behavior approximately conforms to the expected exponential time-dependent evolution of postseismic deformation, indicating that the results are robust although a relatively strong smoothing factor was adopted in the Sentinel-1 time series (e.g., Wang & Fialko, 2018). Both ALOS-2 and Sentinel-1 data show a comparable cumulative motion of up to ~3 cm in LOS.

3.2.2. Afterslip

Assuming that afterslip is the only mechanism that drives the observed postseismic deformation, we find that the inferred afterslip is dominated by thrust motion with significant slip in the top 1.5 km of the crust (Figures 3c–3e). Significant slip patches are discretely distributed along the fault strike, constrained by high-gradient deformation regions. The maximum cumulative afterslip of 10 cm is located at ~1.5-km depth right beneath the maximum coseismic slip zone. The first-order postseismic displacements can be reasonably predicted by the afterslip-only model, yielding an RMS misfit of 2.6 and 3 mm for Sentinel-1 and ALOS-2 data, respectively. The unmodeled signals are primarily observed near the fault bends on the central segment of the fault. The cumulative postseismic moment release is 9.12×10^{16} N m, corresponding to M_w 5.25, which is about 6% of the coseismic moment. The total seismic moment released by aftershocks during the InSAR observation period is about 4×10^{14} N m accounting for only 0.4% of the geodetic moment. Therefore, most postseismic moment was released aseismically.

3.2.3. Poroelastic Rebound Model

Pressure-change induced fluid flow in the shallow crust can produce substantial deformation in the near field (Jónsson et al., 2003). Figures 3f and 3g show that forward models of poroelastic rebound contribute primarily to the near-fault displacements, and its amplitude is proportional to the difference in drained and undrained Poisson's ratios (Figures S8 and S9). Considering that the poroelastic relaxation contributes most to the vertical displacement (Figure S10) and our data are dominated by uplift, we select a poroelastic rebound model with a difference between undrained and drained Poisson's ratio of 0.06 that provides the

best fit (Figures 3f and 3g). The estimated difference in Poisson's ratios is consistent with that of previously published studies (Table S5; see also Fialko, 2004; Fielding et al., 2009; Jónsson et al., 2003; Peltzer et al., 1998; Wang & Fialko, 2018). The maximum estimated value of 1.2 and 1.3 cm for Sentinel-1 and ALOS-2 data seen near the bends along the fault agrees well with the observations (Figures 3a and 3b). The RMS misfits of the rebound-only model are 2.8 and 3.8 mm for the Sentinel-1 and ALOS-2 data, respectively. The large residuals suggest that the poroelastic rebound-only model cannot fully explain the large off-fault displacement in the hanging wall.

3.2.4. Combined Poroelastic and Afterslip Model

We examine whether the observed cumulative postseismic displacement can be even better explained by a model of combined poroelastic rebound and afterslip. We first subtracted the best fitting poroelastic rebound model from the cumulative postseismic observations and then inverted the residuals for the aseismic afterslip following the same method used in the coseismic slip modeling. The afterslip in the combined model is characterized by four major discrete slip patches (Figures 3h–3j). Two afterslip patches appear surrounding the maximum coseismic rupture zone, while the others are located near the edges of the main rupture zone. The maximum cumulative afterslip in the combined model reaches ~8 cm with a seismic moment of 6.27×10^{16} N m, corresponding to an M_w 5.13 event. The combined model well explains the cumulative postseismic LOS displacements in both ascending and descending orbits. The RMS misfits are reduced to 2.3 and 2.9 mm for the Sentinel-1 and ALOS-2 observations, respectively.

4. Discussion

4.1. Causes of Shallow Earthquakes in the Petermann Ranges

Although there is currently no widely accepted mechanism to explain the occurrence of intraplate earthquakes (Calais et al., 2016), significant intraplate seismicity is often observed along ancient preexisting plate boundary zones (Xu et al., 2015) or near steep gradients in the thickness of the lithosphere (Mooney et al., 2012). Here, heterogeneity in strength and stress and the preexistence of large fault structures may provide suitable conditions for intraplate failure. Geological investigations show that the Petermann Ranges represent a Proterozoic-Cambrian plate boundary along which the Musgrave block converged with the Amadeus basin during the upper Proterozoic (Davidson, 1973). The 2016 event and other historic seismicity around the Petermann Ranges likely represent reactivation of ancient fault structures within a larger high strain zone. Also, evidence from gravity and magnetic data shows that there could be a substantial difference in lithosphere thickness beneath the Petermann Ranges (Aitken et al., 2009) where seismicity may be enhanced by the resulting stress heterogeneity. Moreover, the maximum principal stresses in the top several kilometers of crust are oriented approximately north-northeast and horizontal, of high magnitude, and indicate a high deviatoric stress regime (Clark & Mccue, 2003). As suggested by Clark and Mccue (2003), such stress-field conditions may be conducive to shallow rupture initiation. However, the absence of detectable strain accumulation in central Australia (Tregoning, 2003) makes it difficult to relate the intraplate earthquakes to tectonic loading alone (Calais et al., 2016).

Surface faulting earthquakes in Australia appear to occur preferentially on a few preexisting and ancient faults (Clark & Mccue, 2003). These fault zones may represent comparatively permeable layers (Crone, 2003), and may lend themselves to transient weakening by diffusive pore pressure increases in response to rises in precipitation and groundwater level, which reduce the effective normal stress on the fault (e.g., Christiansen et al., 2007; Hainzl et al., 2006). Even small stress perturbations due to environmental changes may bring the prestressed lithosphere to brittle failure (Calais et al., 2016), locally releasing the elastic strain energy accumulated over long intervals.

To investigate the possibility of triggering mechanism of groundwater-level changes, we first estimate the groundwater storage changes in Australia using the GRACE data from 2002–2016 (Tapley et al., 2004; Wahr et al., 1998; Xie et al., 2018), and then convert them into groundwater level changes (Text S3; see also Bear, 2013). The GRACE-derived groundwater-level changes are then combined with in situ well data (https://nt.gov.au/) to investigate the mechanisms of shallow seismicity in the Petermann Ranges. We find that seismicity and the groundwater level changes recorded by GRACE and well data in the Petermann Ranges and in other seismic cluster regions in Australia appear correlated (Figures 4b and S11). Although there are many fluctuations and local highs that are not followed by seismicity, the seismicity around the
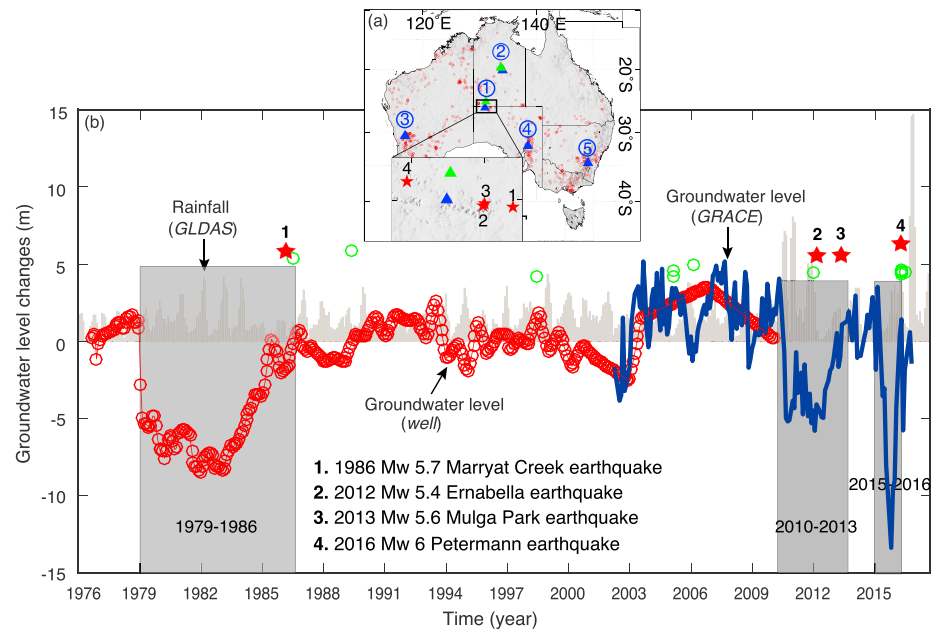
Figure 4. (a) Seismicity cluster regions in Australia numbered from 1 to 5. Green triangles show the locations of ground-water wells (Table S6); blue triangles show sites where water level changes are estimated from the GRACE data. Red circles represent $M \geq 2$ earthquakes since 1910 (https://earthquake.usgs.gov/). Red stars in the inset map show $M_w > 5$ events in the Petermann Ranges numbered from 1 to 4 (Table S1). (b) Relationship between relative "groundwater level" variations and seismicity in the Petermann Ranges (cluster region 1). Red circles represent the groundwater levels from an in situ well, blue line the GRACE solutions. Gray bars showing the precipitation as a three-month moving window in monthly steps (unit in cm) from GLDAS (https://disc.gsfc.nasa.gov). Red stars represent the $M_w > 5$ events shown in (a). Green open circles represent regional $m_b > 4$ seismicity around the Petermann Ranges. The gray regions show the periods with large "groundwater level" fluctuations.

Petermann Ranges tends to accelerate when the groundwater reaches a local maximum level, except in 2010–2013 (Figure 4b). Meanwhile, the magnitude of triggered earthquakes seems to be proportional to the amplitude of fluctuations prior to the events with the 2016 event being preceded by the largest fluctuations. These processes suggest that a transient increase in the elevation of water table might be transmitted downward into the permeable upper crust though pore pressure diffusion (Costain et al., 1987) and lead to an increase of the pore fluid pressure around the fault zone, thus weakening the fault. The hydrologically induced pore pressure variations are primarily limited to the shallow depths of 0–5 km (Hainzl et al., 2006). This is consistent with the shallow events that occurred around the Petermann Ranges, whose hypocentral depths are typically less than 5 km (Table S1). The deeper portions of the ancient faults may be effectively healed, and may not anymore represent preexisting faults that could easily slip. Also, the ambient stress may simply not be high enough at greater depths to produce seismic ruptures. The heterogeneous permeability structure around fault zones could provide the primary control on fluid flow in the upper crust (Caine et al., 1996) and thus determine the relationship between groundwater-level changes and seismic activity. The 2012 M_w 5.4 Ernabella earthquake (event 2 in Figure 4) possibly occurred in a low permeability and porosity fault zone that would cause a time lag with respect to the local groundwater maximum, indicating that the process of fault weakening in the low-permeability fault zone could be delayed (Christiansen et al., 2007). Nevertheless, the low number of events and complex permeability structure challenge our ability to establish a unique causal relationship between groundwater levels and the shallow earthquakes.

Other external environment changes such as nontidal ocean and various other types of surface loads and thermoelastic strain (e.g., Calais et al., 2016; Johnson et al., 2017) may also contribute to time-dependent stress in the study area, but are less obviously linked to the very shallow faulting environment. However, we acknowledge that the spatial and temporal resolution of the GRACE and in situ well data are limited and we cannot perform a quantitative analysis (at least a robust one) on the relationship between groundwater levels and shallow earthquakes based on the current data used. A better understanding

4.2. Possible Mechanisms Driving the Postseismic Process

We show that the afterslip-only model can capture the first-order features of the postseismic signals, but apparent discrepancies are observed near fault bends where high gradients of postseismic deformation are found. Previous studies show that shallow crustal rocks at fault bends of the coseismic rupture usually show a significant change in mechanical properties due to the response to high pore pressure gradients produced by the earthquake (Fielding et al., 2009; Peltzer et al., 1998). This could necessarily result in obvious surface deformation near fault bends in the top ~5 km of the crust (Fielding et al., 2009; Peltzer et al., 1998). The apparent discrepancies between postseismic observations and afterslip predictions led us to consider that poroelastic rebound was involved in the postseismic relaxation of the 2016 Petermann earthquake. The poroelastic rebound-only model with a 0.06 difference in drained and undrained Poisson's ratios explains some details of the localized high-gradient postseismic deformation, but underestimates the off-fault deformation in the hanging wall of the central fault segment. The off-fault deformation does not seem to involve postseismic slip on the shallow secondary faults. Therefore, more than one mechanism is required to fully explain the observed postseismic deformation. The combined poroelastic rebound and afterslip model well reproduces the observed cumulative postseismic LOS displacements resulting in the lowest RMS misfit for both the Sentinel-1 and ALOS-2 data. The combined model maximizes the possible contributions of poroelastic rebound, assuming that they were effectively completed by the end of the Sentinel-1 observation period.

Interestingly, both the afterslip-only model and the combined model suggest that there is a large overlap between the coseismic and postseismic slip on the main fault at the shallow depth (Figure 3). This contrasts to the common understanding that afterslip should be distributed in an upper creeping and/or a deep ductile zone bounding the seismogenic layer or on velocity-strengthening portions of a fault surrounding the rupture asperity (Hsu et al., 2006; Scholz, 1998). However, spatial overlap of coseismic and postseismic slip have also been suggested for other intraplate earthquakes, such as the 1978 M_w 7.3 Tabas earthquake (Zhou et al., 2018) and 2009 M_w 6.3 Dachaidan earthquake (Liu et al., 2016). This phenomenon has been proposed to relate to nonsteady state frictional behavior (Helmstetter & Shaw, 2009) or residual stress heterogeneities that can drive continued slow slip on low-slip rupture zone patches. Theoretical and numerical studies show that the recovery of pore pressure changes can also produce an increment of sympathetic normal stress on the main rupture area and result in fault reloading (Rice, 1980). In addition, the afterslip model suggests spatially heterogeneous material properties around the fault zones that vary either in permeability or porosity. The overlapping or very close coseismic and postseismic slip zones indicates that the behavior of postseismic slip may be tightly coupled with pore fluid flow affecting the frictional strength across various scales in fault zones (Luo & Ampuero, 2017). This pore fluid flow is likely related to poroelastic rebound due to the high coseismic pore pressure gradients.

5. Conclusions

In this study, we investigate the 2016 Petermann Ranges earthquake, central Australia using multiple sources of data. The coseismic slip is mainly concentrated at shallow depths of 0–3 km dominated by thrust-slip motion. This event may have been triggered by transient pore pressure increases associated with rising groundwater levels. A combination of poroelastic rebound and afterslip seems to be the most plausible mechanism that drives the observed postseismic surface deformation. The inferred spatial overlapping of coseismic and postseismic slip indicates that the postseismic slip is tightly coupled with the pore fluid flow and may reflect complex and spatially heterogeneous frictional fault properties.

References

Aitken, A. R. A, Betts, P. G., & Ailleres, L. (2009). The architecture, kinematics, and lithospheric processes of a compressional intraplate orogen occurring under Gondwana assembly: The Petermann orogeny, central Australia. *Lithosphere*, *1*(6), 343–357. https://doi.org/10.1130/L39.1

Bear, J. (2013). *Dynamics of Fluids in Porous Media* (p. 800). Courier Corporation, Technology & Engineering.

Berardino, P., Fornaro, G., Lanari, R., & Sansosti, E. (2002). A new algorithm for surface deformation monitoring based on small baseline differential SAR interferograms. *IEEE Transactions on Geoscience and Remote Sensing*, *40*(11), 2375–2383. https://doi.org/10.1109/TGRS.2002.803792

Caine, J. S., Evans, J. P., & Forster, C. B. (1996). Fault zone architecture and permeability structure. *Geology*, *24*(11), 1025–1028. https://doi.org/10.1130/0091-7613(1996)024<1025:FZAAPS>2.3.CO;2

Calais, E., Camelbeeck, T., Stein, S., Liu, M., & Craig, T. J. (2016). A new paradigm for large earthquakes in stable continental plate interiors. *Geophysical Research Letters*, *43*, 10,621–10,637. https://doi.org/10.1002/2016GL070815

Christiansen, L. B., Hurwitz, S., & Ingebritsen, S. E. (2007). Annual modulation of seismicity along the San Andreas Fault near Parkfield, CA. *Geophysical Research Letters*, *34*, L04306. https://doi.org/10.1029/2006GL028634

Clark, D., & Mccue, K. (2003). Australian paleoseismology: Towards a better basis for seismic hazard estimation. *Annales de Geophysique*, *46*, 1087–1105.

Clark, D., & McPherson, A. (2013). A tale of two seisms: Ernabella 23/03/2012 (M_w5.4) and Mulga Park 09/06/2013 (M_w 5.6). *Australian Earthquake Engineering Society Newsletter*, *2013*, 7–11.

Clark, D., McPherson, A., Allen, T., & De Kool, M. (2014). Coseismic surface deformation caused by the 23 March 2012 M_w 5.4 Ernabella (pukatja) earthquake, central Australia: Implications for fault scaling relations in cratonic settings. *Bulletin of the Seismological Society of America*, *104*(1), 24–39. https://doi.org/10.1785/0120120361

Costain, J. K., Bellinger, G. A., & Speer, J. A. (1987). Hydroseismicity—a hypothesis for the role of water in the generation of intraplate seismicity. *Geology*, *15*, 303–309.

Crone, A. J. (2003). Paleoseismicity of two historically quiescent faults in Australia: Implications for fault behavior in stable continental regions. *Bulletin of the Seismological Society of America*, *93*(5), 1913–1934. https://doi.org/10.1785/0120000094

Davidson, D. (1973). Plate tectonics model for the musgrave block—Amadeus basin complex of central Australia. *Nature*, *245*, 21–23.

Dawson, J., Cummins, P., Tregoning, P., & Leonard, M. (2008). Shallow intraplate earthquakes in Western Australia observed by interferometric synthetic aperture radar. *Journal of Geophysical Research*, *113*, B11408. https://doi.org/10.1029/2008JB005807

Fialko, Y. (2004). Evidence of fluid-filled upper crust from observations of postseismic deformation due to the 1992 M_w7.3 Landers earthquake. *Journal of Geophysical Research*, *109*, B08401. https://doi.org/10.1029/2004JB002985

Fielding, E. J., Lundgren, P. R., Bürgmann, R., & Funning, G. J. (2009). Shallow fault-zone dilatancy recovery after the 2003 Bam earthquake in Iran. *Nature*, *458*(7234), 64–68. https://doi.org/10.1038/nature07817

Gold, R., Clark, D., King, T., & Quigley, M. (2017). *Surface rupture and vertical deformation associated with 20 May 2016 M*6 Petermann Ranges earthquake (Vol. 19). Northern Territory, Australia: EGU General Assembly Conference.

Gordon, R. G. (1998). The plate tectonic approximation: Plate nonrigidity, diffuse plate boundaries, and global plate reconstructions. *Annual Review of Earth and Planetary Science*, *26*(1), 615–642. https://doi.org/10.1146/annurev.earth.26.1.615

Hainzl, S., Kraft, T., Wassermann, J., Igel, H., & Schmedes, E. (2006). Evidence for rainfall-triggered earthquake activity. *Geophysical Research Letters*, *33*, B04203. https://doi.org/10.1029/2006GL027642

Helmstetter, A., & Shaw, B. E. (2009). Afterslip and aftershocks in the rate-and-state friction law. *Journal of Geophysical Research*, *114*, B01308. https://doi.org/10.1029/2007JB005077

Hsu, Y.-J., Simons, M., Avouac, J. P., Galetzka, J., Sieh, K., Chlieh, M., et al. (2006). Frictional afterslip following the 2005 Nias-Simeulue earthquake, Sumatra. *Science*, *312*(5782), 1921–1926. https://doi.org/10.1126/science.1126960

Huang, H., Xu, W., Meng, L., Bürgmann, R., & Baez, J. C. (2017). Early aftershocks and afterslip surrounding the 2015 M_w 8.4 Illapel rupture. *Earth and Planetary Science Letters*, *457*, 282–291. https://doi.org/10.1016/j.epsl.2016.09.055

Johnson, C. W., Fu, Y., & Bürgmann, R. (2017). Stress models of the annual hydrospheric, atmospheric, thermal, and tidal loading cycles on California faults: Perturbation of background stress and changes in seismicity. *Journal of Geophysical Research: Solid Earth*, *122*, 10–605. https://doi.org/10.1002/2017JB014778

Jónsson, S., Segall, P., Pedersen, R., & Björnsson, G. (2003). Post-earthquake ground movements correlated to pore-pressure transients. *Nature*, *424*(6945), 179–183. https://doi.org/10.1038/nature01776

Jónsson, S., Zebker, H., Segall, P., & Amelung, F. (2002). Fault slip distribution of the 1999 M_w 7.1 Hector Mine, California, earthquake, estimated from satellite radar and GPS measurements. *Bulletin of the Seismological Society of America*, *92*(4), 1377–1389. https://doi.org/10.1785/0120000922

King, T. R., Quigley, M. C., & Clark, D. (2018). Earthquake environmental effects produced by the M_w 6.1, 20th May 2016 Petermann earthquake, Australia. *Tectonophysics*, *747*, 357–372. https://doi.org/10.1016/j.tecto.2018.10.010

Leonard, M., Burbidge, D. R., Allen, T. I., Robinson, D. J., McPherson, A., Clark, D., & Collins, C. D. N. (2014). The challenges of probabilistic seismic-hazard assessment in stable continental interiors: An Australian example. *Bulletin of the Seismological Society of America*, *104*(6), 3008–3028. https://doi.org/10.1785/0120130248

Liu, Y., Xu, C., Li, Z., Wen, Y., Chen, J., & Li, Z. (2016). Time-dependent afterslip of the 2009 M_w 6.3 Dachaidan earthquake (China) and viscosity beneath the Qaidam Basin inferred from postseismic deformation observations. *Remote Sensing*, *8*(8), 649. https://doi.org/10.3390/rs8080649

Luo, Y., & Ampuero, J. P. (2017). Stability of faults with heterogeneous friction properties and effective normal stress. *Tectonophysics*, *733*, 257–272. https://doi.org/10.1016/j.tecto.2017.11.006

Maerten, F., Resor, P., Pollard, D., & Maerten, L. (2005). Inverting for slip on three-dimensional fault surfaces using angular dislocations. *Bulletin of the Seismological Society of America*, *95*(5), 1654–1665. https://doi.org/10.1785/0120030181

Massonnet, D., Rossi, M., Carmona, C., Adragna, F., Peltzer, G., Feigl, K., & Rabaute, T. (1993). The displacement field of the Landers earthquake mapped by radar interferometry. *Nature*, *364*(6433), 138–142. https://doi.org/10.1038/364138a0

Meade, B. J. (2007). Algorithms for the calculation of exact displacements, strains, and stresses for triangular dislocation elements in a uniform elastic half space. *Computers & Geosciences*, *33*(8), 1064–1075. https://doi.org/10.1016/j.cageo.2006.12.003

Mooney, W. D., Ritsema, J., & Hwang, Y. K. (2012). Crustal seismicity and the earthquake catalog maximum moment magnitude (Mcmax) in stable continental regions (SCRs): Correlation with the seismic velocity of the lithosphere. *Earth and Planetary Science Letters*, *357*, 78–83.

Pain, C. F., Villans, B. J., Roach, I. C., Worrall, L., & Wilford, J. R. (2012). Old, flat and red—Australia's distinctive landscape. In R. S. Blewitt (Ed.), *Shaping a Nation: A Geology of Australia* (pp. 227–275). Canberra: Geoscience Australia and ANU E Press. ISBN 978–1–922103-43-7

Parsons, B., Wright, T., Rowe, P., Andrews, J., Jackson, J., Walker, R., et al. (2006). The 1994 Sefidabeh (eastern Iran) earthquakes revisited: New evidence from satellite radar interferometry and carbonate dating about the growth of an active fold above a blind thrust fault. *Geophysical Journal International*, *164*(1), 202–217. https://doi.org/10.1111/j.1365-246X.2005.02655.x

Peltzer, G., Rosen, P., Rogez, F., & Hudnut, K. (1998). Poroelastic rebound along the Landers 1992 earthquake surface rupture. *Journal of Geophysical Research*, *103*(B12), 30,131–30,145. https://doi.org/10.1029/98JB02302

Polcari, M., Albano, M., Atzori, S., Bignami, C., & Stramondo, S. (2018). The causative fault of the 2016 M_{wp} 6.1 Petermann Ranges intraplate earthquake (central Australia) retrieved by C-and L-band InSAR data. *Remote Sensing*, *10*(8), 1311. https://doi.org/10.3390/rs10081311

Rajabi, M., Tingay, M., Heidbach, O., Hillis, R., & Reynolds, S. (2017). The present-day stress field of Australia. *Earth Science Reviews*, *168*, 165–189. https://doi.org/10.1016/j.earscirev.2017.04.003

Rice, J. R. (1980). The mechanics of earthquake rupture. In A. M. Dziewonski & E. Boschi (Eds.), *Physics of the Earth's Interior* (pp. 555–649). Amsterdam: North-Holland.

Schmidt, D. A., & Bürgmann, R. (2003). Time-dependent land uplift and subsidence in the Santa Clara valley, California, from a large interferometric synthetic aperture radar data set. *Journal of Geophysical Research*, *108*(B9), 2416. https://doi.org/10.1029/2002JB002267

Scholz, C. H. (1998). Earthquakes and friction laws. *Nature*, *391*(6662), 37–42. https://doi.org/10.1038/34097

Tapley, B. D., Bettadpur, S., Ries, J. C., Thompson, P. F., & Watkins, M. M. (2004). GRACE measurements of mass variability in the Earth system. *Science*, *305*(5683), 503–505. https://doi.org/10.1126/science.1099192

Tregoning, P. (2003). Is the Australian plate deforming? A space geodetic perspective. *Geological Society of America Special Papers*, *372*, 41–48.

Wahr, J., Molenaar, M., & Bryan, F. (1998). Time variability of the Earth's gravity field: Hydrological and oceanic effects and their possible detection using GRACE. *Journal of Geophysical Research*, *103*(B12), 30,205–30,229. https://doi.org/10.1029/98JB02844

Wang, K., & Fialko, Y. (2018). Observations and modeling of coseismic and postseismic deformation due to the 2015 M_w 7.8 Gorkha (Nepal) earthquake. *Journal of Geophysical Research: Solid Earth*, *123*, 761–779. https://doi.org/10.1002/2017JB014620

Wang, S., Xu, C., Wen, Y., Yin, Z., Jiang, G., & Fang, L. (2017). Slip model for the 25 November 2016 M_w 6.6 Aketao earthquake, Western China, revealed by Sentinel-1 and ALOS-2 observations. *Remote Sensing*, *9*(4), 325. https://doi.org/10.3390/rs9040325

Wessel, P., Smith, W. H. F., Scharroo, R., Luis, J., & Wobbe, F. (2013). Generic Mapping Tools: Improved version released. *Eos, Transactions of the American Geophysical Union*, *94*(45), 409–410. https://doi.org/10.1002/2013EO450001

Xie, X., Xu, C., Wen, Y., & Li, W. (2018). Monitoring groundwater storage changes in the loess plateau using grace satellite gravity data, hydrological models and coal mining data. *Remote Sensing*, *10*(4), 605. https://doi.org/10.3390/rs10040605

Xu, W. (2017). Finite-fault slip model of the 2016 M_w 7.5 Chiloé earthquake, southern Chile, estimated from Sentinel-1 data. *Geophysical Research Letters*, *44*, 4774–4780. https://doi.org/10.1002/2017GL073560

Xu, W., Dutta, R., & Jónsson, S. (2015). Identifying active faults by improving earthquake locations with InSAR data and Bayesian estimation: The 2004 Tabuk (Saudi Arabia) earthquake sequence. *Bulletin of the Seismological Society of America*, *105*, 1–12.

Xu, W., Feng, G., Meng, L., Zhang, A., Ampuero, J. P., Bürgmann, R., & Fang, L. (2018). Transpressional rupture cascade of the 2016 M_w 7.8 Kaikoura earthquake, New Zealand. *Journal of Geophysical Research: Solid Earth*, *123*, 2396–2409. https://doi.org/10.1002/2017JB015168

Yin, Z., Xu, C., Wen, Y., Jiang, G., Fan, Q., & Liu, Y. (2016). A new hybrid inversion method for parametric curved faults and its application to the 2008 Wenchuan (China) earthquake. *Geophysical Journal International*, *205*(2), 954–970. https://doi.org/10.1093/gji/ggw060

Zhao, B., Bürgmann, R., Wang, D., Tan, K., Du, R., & Zhang, R. (2017). Dominant controls of downdip afterslip and viscous relaxation on the postseismic displacements following the M_w7.9 Gorkha, Nepal, earthquake. *Journal of Geophysical Research: Solid Earth*, *122*, 8376–8401. https://doi.org/10.1002/2017JB014366

Zhou, Y., Thomas, M. Y., Parsons, B., & Walker, R. T. (2018). Time-dependent postseismic slip following the 1978 M_w 7.3 Tabas-e-Golshan, Iran earthquake revealed by over 20 years of ESA InSAR observations. *Earth and Planetary Science Letters*, *483*, 64–75. https://doi.org/10.1016/j.epsl.2017.12.005